

Modified recombination and the Hubble tension

Seyed Hamidreza Mirpoorian,^{1,*} Karsten Jedamzik,^{2,†} and Levon Pogosian^{1,‡}

¹*Department of Physics, Simon Fraser University, Burnaby, BC, V5A 1S6, Canada*

²*Laboratoire de Univers et Particules de Montpellier, UMR5299-CNRS,
Universite de Montpellier, 34095 Montpellier, France*

(Dated: November 26, 2024)

We investigate the extent to which modifying the ionization history at cosmological recombination can relieve the Hubble tension, taking into account all relevant datasets and considering the implications for the galaxy clustering parameter S_8 and the matter density fraction Ω_m . We use the linear response approximation to systematically search for candidate ionization histories parameterized with a cubic-spline that provide good fits to the Planck CMB and DESI BAO data while relieving the H_0 tension, followed by MCMC fits of the most promising candidate models to the data. We also fit to the data a physically motivated phenomenological model of ionization history that has four parameters. Our main result is that models of modified recombination can reduce the Hubble tension to below 2σ while improving the fit to the current CMB and BAO data and reducing the S_8 tension. The promising candidate ionization histories have simple shapes, with no need for an oscillatory dependence on redshift. Our study also demonstrates the importance of the high-resolution CMB temperature and polarization anisotropies for constraining modified recombination, with the candidate models in this study showing varying levels of agreement with the current ACT DR4 and SPT-3G data.

I. INTRODUCTION

The standard Λ Cold Dark Matter (Λ CDM) model has been very successful in providing a good fit to a wide range of cosmological observations. However, the emergence of tensions between certain datasets interpreted within the Λ CDM framework have prompted discussions of new physics. The most notable of these is the Hubble tension, which reflects a significant discrepancy between the value of the Hubble constant H_0 inferred from the Planck Cosmic Microwave Background (CMB) data, $H_0 = 67.36 \pm 0.54$ km/s/Mpc, and $H_0 = 73.04 \pm 1.04$ km/s/Mpc measured by the SH0ES collaboration using Cepheid-calibrated supernovae Type Ia (SN) [1, 2].

Another noteworthy discrepancy, albeit less severe, concerns measurements of the matter clustering amplitude quantified by the parameter $S_8 \equiv \sigma_8 \sqrt{\Omega_m/0.3}$, where σ_8 is the amplitude of matter density fluctuations smoothed over the scale of 8 Mpc/h, and Ω_m is the present-day matter density fraction of the critical density. In particular, the Planck-CMB-inferred value of $S_8 = 0.832 \pm 0.013$ is 1.9σ higher than the value of $S_8 = 0.790^{+0.018}_{-0.014}$ obtained from galaxy counts and weak lensing through a joint analysis [3] of the Dark Energy Survey Year 3 (DES-Y3) [4] and Kilo-Degree Survey (KiDS-1000) [5] data.

An additional minor tension emerged recently between the value of Ω_m deduced from uncalibrated (independent of the intrinsic supernovae brightness) SN luminosity distance vs redshift curves and that obtained from

uncalibrated (independent of the comoving sound horizon at decoupling) Baryon Acoustic Oscillations (BAO) distance measurements. The Pantheon+ (PP) SN data yields $\Omega_m = 0.334 \pm 0.018$ [6], in good agreement with DES-Y5 [7] and Union3 [8] SN datasets, while the recent BAO measurements by the Dark Energy Spectroscopic Instrument (DESI) give $\Omega_m = 0.295 \pm 0.015$ [9]. Although only at a $\sim 2\sigma$ level, this tension adds an interesting consideration to the discussion of cosmological tensions because it is independent of the calibration of either SN or BAO.

While the possibility of unaccounted systematic effects cannot be ruled out, no single source of systematics has been identified so far that could resolve the Hubble tension [10–13] or explain the more mild S_8 and the Ω_m discrepancies. Naturally, the above tensions, especially the Hubble tension, have raised significant interest in potential new physics beyond the Λ CDM model. Proposed solutions to the Hubble tension are often categorized into late-time and early-time modifications [14–16]. Late-time solutions, such as dynamical dark energy, interacting dark matter and dark energy, modified gravity, and decaying dark matter, generally struggle to resolve the tension due to the strong constraints from the BAO and SN data [17–22]. As a result, many researchers are focusing on the early-time solutions that reduce the comoving sound horizon r_* at photon-baryon decoupling by either increasing the energy density of the Universe prior to recombination or increasing the rate of recombination. These include models of early dark energy (EDE), interacting neutrinos, varying fundamental constants, primordial magnetic fields (PMF) and others [16]. In particular, stochastic PMF naturally speed up recombination by inducing small-scale inhomogeneities in the baryon density prior recombination, helping relieve both the H_0 and S_8 tensions [23–25].

*smirpoor@sfu.ca

†karsten.jedamzik@umontpellier.fr

‡levon.pogosian@sfu.ca

In this paper, motivated by the PMF proposal, we investigate to what extent a modification of the recombination history can help resolve the Hubble tension without exacerbating the other tensions. Related studies were performed in [26–28]. In [26], Lee *et al* modified recombination by allowing the electron mass m_e to be a free function of redshift z . They used the linear response approximation (LRA) method to search for $m_e(z)$ that yield a Planck CMB best fit value of $H_0 = 73.04$ km/s/Mpc with the same Planck χ^2 as the standard Λ CDM fit. They found that there are indeed modified recombination histories that allow for this, but not when the BAO data is added to CMB. The latter is expected, since CMB and BAO are generally consistent with each other within the standard recombination model (see [29] for a recent analysis of this), while requiring a different adjustment of r_* in order to get $H_0 = 73.04$ km/s/Mpc [30]. Nevertheless, Lee *et al* found recombination histories that significantly reduce the Hubble tension while still providing acceptable fits to both CMB and BAO. In [27, 28], Lynch *et al* fit a cubic spline parametrization of the ionized fraction, $x_e(z)$, to the combination of Planck and DESI BAO (without a SH0ES prior on H_0) and found that this yields $H_0 = 70 \pm 1.1$ km/s/Mpc, providing a considerable reduction of the Hubble tension.

Our study builds on the approaches of [26–28] in two ways. First, we revisit the LRA method used in [26] and, instead of m_e , vary $x_e(z)$ directly to systematically search for parameter combinations that yield $H_0 > 70$ km/s/Mpc, while improving the χ^2 and reducing the value of S_8 . We find that one can have $H_0 \sim 71$ km/s/Mpc with a lower CMB+BAO χ^2 than the Λ CDM best fit. The LRA method, as well as the cubic spline parametrization of [27, 28], yield wiggly $x_e(z)$ that would be difficult to realize in a physical system. It was interesting to understand if having the wiggles is necessary for achieving a high value of H_0 and to what extent. To address this question, we introduce a simple four-parameter model of $x_e(z)$ that can approximately match the recombination histories predicted by PMF and fit it to the data. We find that one can in fact get $H_0 \sim 71$ km/s/Mpc without the wiggles in $x_e(z)$, while improving the CMB+BAO fit and reducing the S_8 tension. We also demonstrate the important role of small-scale CMB temperature and polarization anisotropy spectra in discriminating between different modified recombination models.

In what follows, Section II introduces our LRA-based parameter search and the 4-parameter model, Section III describes the datasets used in the analysis, followed by the results presented in Section IV and a discussion in Section V. We conclude with a brief summary in Section VI. Additional analysis details and results are presented in the Appendices.

II. METHODOLOGY

The more successful theoretical proposals to resolve the Hubble tension involve reducing the comoving sound

horizon at the photon-baryon decoupling, r_* . This shifts the acoustic peaks in the CMB and matter power spectra to smaller scales, requiring a reduction in the comoving distance to the redshift of decoupling, and hence a larger H_0 , in order to preserve the observed angular scales of the acoustic features. The sound horizon is computed as

$$r_* = \int_{z_*}^{\infty} \frac{c_s(z)}{H(z)} dz, \quad (1)$$

where $c_s(z)$ is the sound speed of the baryon-photon fluid, $H(z)$ is the redshift-dependent cosmological expansion rate, and z_* is the redshift of decoupling that depends on the recombination history. The latter is described by the ionized fraction $x_e(z)$, defined as

$$x_e(z) = \frac{n_e}{n_H}, \quad (2)$$

where n_e is the number density of free electrons, and n_H is the total number density of hydrogen nuclei in the primordial plasma. The ionization fraction determines the differential optical depth $\hat{\tau}$, given by $\hat{\tau} = \sigma_T n_e a$, where σ_T is the Thomson scattering cross-section, and a is the scale factor. The visibility function, which describes the probability of last photon scattering at a given redshift, is given by $g(z) \equiv \hat{\tau} e^{-\hat{\tau}}$. The peak of the visibility function defines the redshift of photon decoupling, z_* , which sets the bound in the integral (1) and marks the time when photons last scattered and the CMB was released [31]. Thus, a change in $x_e(z)$ would affect z_* and, therefore, r_* and the inferred value of H_0 .

We adopt two distinct yet complementary approaches to modifying the ionization history in order to address cosmological tensions, with a particular focus on the Hubble tension. First, we use the LRA method to search in a systematic way for small changes in the ionization fraction $x_e(z)$ across a broad redshift range that help relieve the H_0 and S_8 tensions while maintaining a good fit to the CMB and BAO data. Then we consider a 4-parameter model of $x_e(z)$ motivated by baryon clumping models in the studies of PMF. Both approaches are designed to assess the extent to which modifications to the recombination history can relieve the Hubble tension in a model-agnostic way.

A. The linear response approximation (LRA) method

One way to search for modified recombination histories that solve the Hubble tension is by adopting a flexible parameterization of $x_e(z)$, *e.g.* a cubic spline with many nodes, and fitting it to data to explore the acceptable parameter space. In practice, this is computationally expensive, and can be plagued by degeneracies due to the large number of correlated parameters. One can address the computational cost through the use of emulators, as was done in [27, 28]. Still, this procedure would only

provide a best fit and marginalized posterior distributions for the $x_e(z)$ parameters, potentially missing viable $x_e(z)$ shapes that give acceptable fits but not necessarily the best fit.

The LRA method offers a quick way to search in a systematic way for all acceptable $x_e(z)$. It employs the Fisher approximation to compute the changes in the minimum χ^2 due to small changes in parameters around a given fiducial model. The parameters could include nodes of a smooth function, such as $x_e(z)$, making it possible to predict how a change in $x_e(z)$ would affect the χ^2 without the computational cost of performing a MCMC fit to the data. The limitation of the LRA method is that the accuracy of the prediction is reduced when departures from the fiducial model are large. However, one can always test the quality of the predictions by fitting a few predictions that are of special interests to the data, which is the approach we take in this study.

A general observable can be represented by a vector \mathbf{X} , which may consist of multiple observables such as the CMB temperature and polarization power spectra, BAO measurements, *etc.* In our analysis, \mathbf{X} includes the Planck CMB temperature and polarization spectra, and the BAO measurements from DESI. The theoretical prediction \mathbf{X}^{th} depends on a set of standard cosmological parameters given by a vector $\vec{\Omega} \equiv \{\Omega_c h^2, \Omega_b h^2, H_0, \tau, \log(10^{10} A_s), n_s\}$. Assuming a Gaussian likelihood, the χ^2 for a theoretical model can be written as

$$\chi^2(\vec{\Omega}) = \left[\mathbf{X}^{\text{th}}(\vec{\Omega}) - \mathbf{X}^{\text{obs}} \right] \cdot \mathbf{M}(\vec{\Omega}) \cdot \left[\mathbf{X}^{\text{th}}(\vec{\Omega}) - \mathbf{X}^{\text{obs}} \right], \quad (3)$$

where \mathbf{X}^{obs} is the observed data vector, and $\mathbf{M} = \boldsymbol{\Sigma}^{-1}$ is the inverse of the covariance matrix. In [26], Lee *et al* have shown that the shifts in the best-fit parameters and χ^2 due to changes in a smooth function can be calculated using integrals involving functional derivatives with respect to that function. Replacing the electron mass $m_e(z)$ with $\ln[x_e(z)]$, and otherwise closely following their formalism, the change in the i -th best-fit parameter Ω_{BF}^i due to a perturbation of the ionization history $\Delta \ln[x_e(z)]$ can be written as

$$\Delta \Omega_{\text{BF}}^i = - \int dz F_{ij}^{-1} \frac{\partial \mathbf{X}}{\partial \Omega^j} \cdot \mathbf{M} \cdot \frac{\delta \mathbf{X}}{\delta \ln[x_e(z)]} \Delta \ln[x_e(z)] \quad (4)$$

where all the quantities inside the integral except $\Delta \ln[x_e(z)]$ are evaluated at the fiducial cosmology that is assumed to be close to the new best-fit. We take the fiducial model as the best-fit Λ CDM model with the conventional recombination history. Here F_{ij} is the Fisher matrix evaluated at the fiducial model given by

$$F_{ij} = \left(\frac{\partial \mathbf{X}}{\partial \Omega^i} \cdot \mathbf{M}(\vec{\Omega}) \cdot \frac{\partial \mathbf{X}}{\partial \Omega^j} \right) \Bigg|_{\text{fid}}. \quad (5)$$

One can also derive an expression for the change in the best-fit chi-squared, $\Delta \chi_{\text{BF}}^2$, due to the perturbation

$\Delta \ln[x_e(z)]$ that we provide in Appendix A 1. The optimization problem then reduces to finding $\Delta \ln[x_e(z)]$ such that $\Delta \chi_{\text{BF}}^2 \leq 0$ while providing a relief of the cosmological tensions. In particular, we will be searching for all $\Delta \ln[x_e(z)]$ that reduce χ_{BF}^2 while predicting $H_0^{\text{BF}} \geq 70$, and $S_8^{\text{BF}} < S_8^{\text{fid}}$.

To evaluate the integral in Eq. (4) and the corresponding integral for $\Delta \chi_{\text{BF}}^2$, first we need to compute the functional derivatives such as $\delta \mathbf{X} / \delta \ln[x_e(z)]$. We evaluate them numerically using the formalism used by Hart *et al* in [32]. Namely, we create an orthonormal set of basis functions of Gaussian shape centered at a set of redshift values z_k to perturb $x_e(z)$ in narrow redshift ranges around z_k . We then implement the perturbed $x_e(z)$ in the recombination routine RECFAST [33–35] of the Boltzmann code CAMB [36] and compute the response of observables \mathbf{X} to the perturbation. Having evaluated all necessary functional derivatives, we can compute $\Delta \Omega_{\text{BF}}^i$ and $\Delta \chi_{\text{BF}}^2$ for any (small) modification of ionization history $\Delta \ln[x_e(z)]$. With this pipeline at hand, we can search for $\Delta \ln[x_e(z)]$ that satisfy our criteria. We do this by generating a large number of $\Delta \ln[x_e(z)]$ histories using cubic splines with 7 control points placed evenly between $z = 700$ and $z = 1600$. Further details of our procedure are given in Appendix A.

The accuracy of the LRA method worsens for best fits that are further away from the fiducial model. To check how well the LRA-predicted best fit ionization histories actually fit the data, we perform MCMC fits in a few particularly interesting cases. In addition to checking how well a given LRA prediction actually fits the combination of Planck CMB and DESI BAO data, we also check the impact of adding the SN data and the high-resolution CMB anisotropy measurements to the dataset.

B. The 4-parameter model

Fully agnostic parameterizations of $x_e(z)$, such as a cubic spline, are helpful for exploring the extent to which modified recombination can relieve the tensions. However, such methods tend to yield best fit ionization histories that would be difficult to realize in a physical system, such as the highly oscillatory $x_e(z)$ obtained in [26–28] and our LRA results presented in Sec. IV. It is, therefore, interesting to know if modifications of simpler shape could help relieve the Hubble tensions at a similar level.

To this end, we adopt a 4-parameter model of $x_e(z)$ motivated by ionization histories obtained from simulations of recombination in the presence of PMF [37]. The model allows for an overall shift of the unmodified ionization history $x_e^{(0)}$ in redshift quantified by dz_{sh} , along with a Gaussian-shape bump at a certain reference redshift z_b of amplitude A_b and a width-at-half-maximum σ_b . It is given by

$$x_e(z) = x_e^{(0)}(z - dz_{\text{sh}}) \left\{ 1 + A_b \exp \left[-\frac{(z - z_b)^2}{2\sigma_b^2} \right] \right\}, \quad (6)$$

where, for a given set of cosmological parameters, $x_e^{(0)}$ is the output of the standard recombination model implemented in **RECFAST**.

III. DATASETS

In this Section we separately describe the datasets in the data vector and the Fisher matrix used in the LRA forecast, and the datasets used in the MCMC analysis when fitting the LRA predictions and the 4-parameter to data.

A. The data vector in the LRA method

The data vector \mathbf{X}^{obs} in our LRA Fisher forecast consists of the Planck CMB temperature and polarization spectra, and the BAO measurements from DESI. We use this combination because the extent to which one can relieve the Hubble tension by reducing the sound horizon is primarily limited by the challenge of maintaining simultaneously good fits to the CMB and BAO data.

1. Planck CMB

We use both the high- ℓ and low- ℓ Planck CMB likelihoods in our LRA Fisher forecast. For $\ell \geq 30$, we use the C_ℓ^{TT} , C_ℓ^{TE} and C_ℓ^{EE} spectra and the covariance matrix from the **Cobaya** [38, 39] implementation of the Planck PR4 CamSpec (NPIPE) likelihood [40]. The high- ℓ CMB part of the data vector in the LRA analysis is given by

$$\mathbf{X}_{\text{high-}\ell}^{\text{obs}} \equiv \left\{ C_{\ell(143)}^{TT}, C_{\ell(217)}^{TT}, C_{\ell(143 \times 217)}^{TT}, C_\ell^{TE}, C_\ell^{EE} \right\}, \quad (7)$$

where we used C_ℓ^{TT} from two high-frequency maps at 143 and 217 GHz, and the 143×217 cross-spectra, with $\ell_{\text{max}} = \{2000, 2500, 2500\}$ respectively. To compute the difference between \mathbf{X}^{obs} in (7) and \mathbf{X}^{th} in (3), one needs to add the contribution from foreground residuals to the fiducial cosmology prediction. We use the expression given by [40]

$$C_\ell^{\text{power}} = A_\nu^{\text{power}} \left(\frac{\ell}{1500} \right)^{\gamma_\nu^{\text{power}}}, \quad (8)$$

where the nuisance parameters A_ν^{power} and $\gamma_\nu^{\text{power}}$ represent the amplitudes and spectral indices of power-law fits to foreground residuals for each of the TT spectra labeled by ν .

For the temperature spectra C_ℓ^{TT} with $\ell < 30$ we use the **Cobaya** implementation of the Planck 2018 baseline low- ℓ TT likelihood [41].

For the $\ell < 30$ E-mode polarization power spectra, we use **Planck-low-py**, a Python-based compressed likelihood introduced by Prince et al. [42], which has been shown to provide constraints on cosmological parameters consistent with the full likelihoods from the Planck

legacy release. In their formalism, the EE spectra are compressed into three bins, and a log-normal distribution is used to approximate the likelihood. The probability distribution for the binned power spectrum $D_\ell^{EE} = \ell(\ell+1)C_\ell^{EE}/2\pi$ is given by

$$\mathcal{L}(x) = \frac{1}{(x-x_0)\sigma\sqrt{2\pi}} \exp \left[-\frac{(\ln(x-x_0)-\mu)^2}{2\sigma^2} \right], \quad (9)$$

where $x = D_{\text{bin}}^{EE}$ with the best-fitting parameters x_0 , μ and σ provided in [42]. We use $\mathbf{X}_{\text{low-}\ell}^{EE} \equiv D_{\text{bin}}^{EE}$ as the low- ℓ EE contribution to the data vector in the LRA analysis.

2. DESI 2024 BAO

We use the DESI Year 1 BAO data [9] comprised of three types of observables: $D_M(z)/r_{\text{drag}}$, $D_H(z)/r_{\text{drag}}$, and $D_V(z)/r_{\text{drag}}$. Here r_{drag} is the sound horizon at the ‘‘baryon drag’’ epoch, with $r_{\text{drag}} \approx 1.02r_*$ in Λ CDM, D_M is the comoving distance to redshift z , $D_H = c/H(z)$, and $D_V(z) = [zD_M^2(z)D_H(z)]^{1/3}$ [43]. The BAO contribution the data vector consists of 12 data points of these three types at 7 effective redshifts, $z_{\text{eff}} = 0.295, 0.510, 0.706, 0.930, 1.317, 1.491, \text{ and } 2.330$, taken from [9].

B. Datasets used in MCMC runs

In our MCMC fits of the 4-parameter model and the ionization histories predicted by the LRA method to the data we use combinations of the following datasets:

- **Planck**: the Planck PR4 CamSpec (NPIPE) likelihood [40] for the $\ell \geq 30$ CMB TT, TE and EE spectra, the Planck 2018 baseline $\ell < 30$ TT and EE likelihoods [41], and the Planck PR4 lensing likelihood [44];
- **DESI**: the 12 BAO measurements at 7 effective redshifts from DESI Year 1 release [9];
- **SPT**: the high-resolution CMB TT, TE, EE spectra from the 2022 release of the South Pole Telescope 3G (SPT-3G) experiment [45];
- **ACT**: high-resolution CMB TT, TE, EE spectra from the 4th data release of the Atacama Cosmology Telescope experiment (ACT-DR4) [46];
- **PP**: The Pantheon+ collection of uncalibrated SN magnitudes [6];
- **PPM_b**: The Pantheon+ (PP) SN dataset [6] calibrated using the brightness magnitude $M_b = -19.253 \pm 0.027$ from the cosmic distance ladder measurement by the SH0ES collaboration [1].

We use **Cobaya** [38, 39] to perform the MCMC analysis.

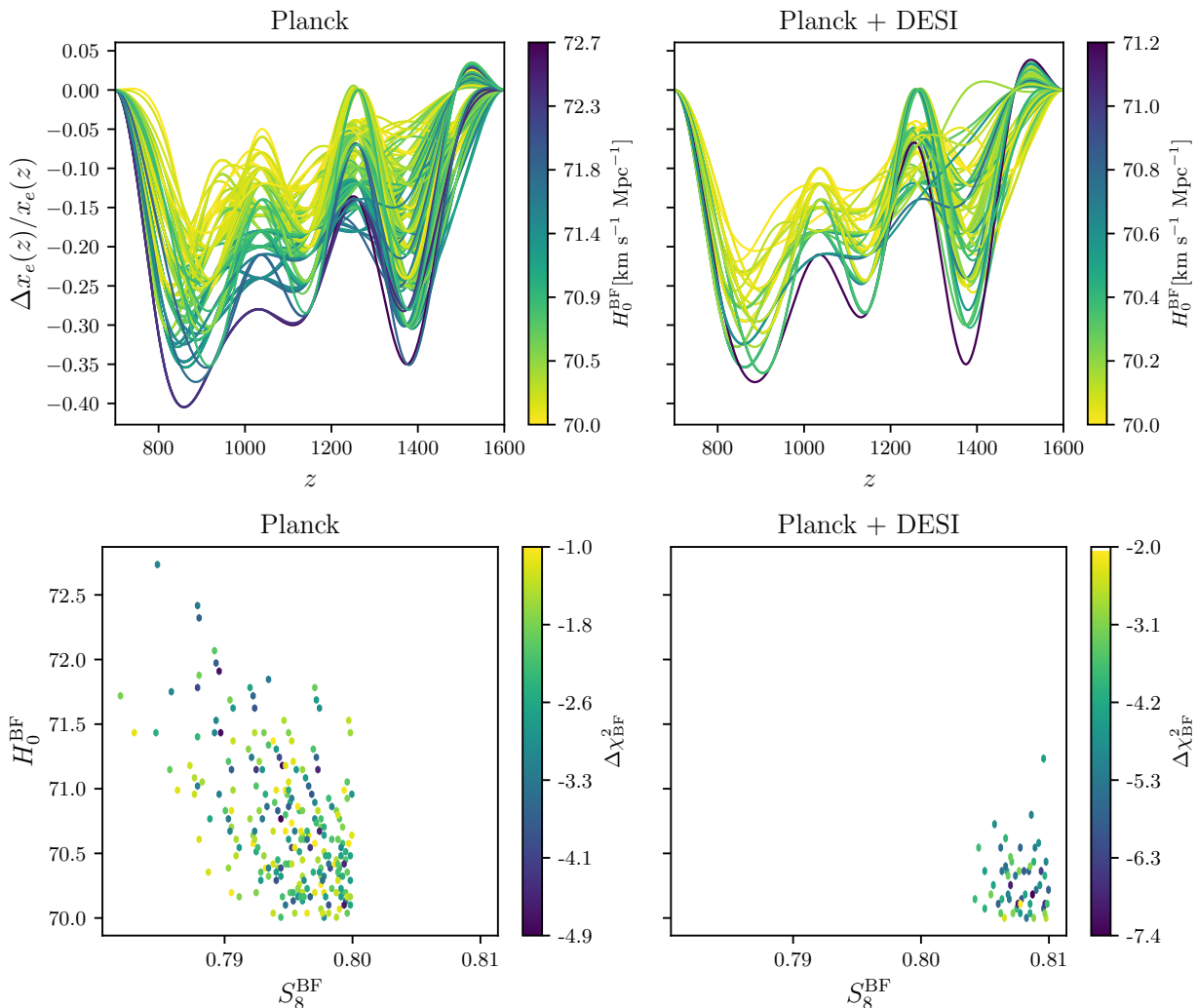


FIG. 1: Top: LRA-predicted ionization histories, plotted in terms of their relative difference from Λ CDM, with the best-fit H_0 values indicated with the color bar, for Planck (left) and Planck + DESI (right). Bottom: the values of H_0 and S_8 for the ionization histories shown in the top panels with the color bar indicating the corresponding $\Delta\chi_{\text{BF}}^2$ values. We restricted our search to models with $S_8^{\text{BF}} < 0.8$ for Planck, and $S_8^{\text{BF}} < 0.81$ for Planck + DESI.

IV. RESULTS

As described in Sec. II A, we use the LRA method to search for $x_e(z)$ that reduce the best-fit Planck and DESI chi-squared relative to the fiducial Λ CDM model, while predicting $H_0^{\text{BF}} \geq 70$ and $S_8^{\text{BF}} < S_8^{\text{fid}}$. We perform this search separately for Planck alone and for the combination of Planck and DESI by generating a large number of ionization histories using cubic splines with 7 control points placed evenly between $z = 700$ and $z = 1600$.

The top panels in Fig. 1 show the recombination histories obtained via the LRA method that satisfy our three criteria with the colors indicating the corresponding values of H_0 . The bottom panels show the distribution of the H_0 and S_8 values for the same histories, with the colors indicating the improvement in χ_{BF}^2 . It is worth noting that the success rate of finding recombination histories

which pass all three criteria was very small, $\sim 0.02\%$ for Planck and $\sim 0.005\%$ for Planck + DESI. This suggests that relieving the Hubble tension requires a very particular modification of the recombination history. It is also apparent that the inclusion of the BAO data yields smaller H_0 and larger S_8 , as expected for reasons presented in [30].

The successful recombination histories in Fig. 1 are generally wiggly. We attribute this, in part, to our choice of the parameterization, *i.e.* using a cubic spline with seven pivot points. As we discuss later in this Section, the presence of the wiggles is not a necessary condition for modified recombination to substantially relieve the H_0 tension.

Next, we select two specific ionization histories obtained from the LRA search: one from the analysis of the best fit to Planck that predicts $H_0 = 71.9$ km/s/Mpc, $S_8 = 0.79$, and $\Delta\chi_{\text{BF}}^2 = -4.71$, and one from the com-

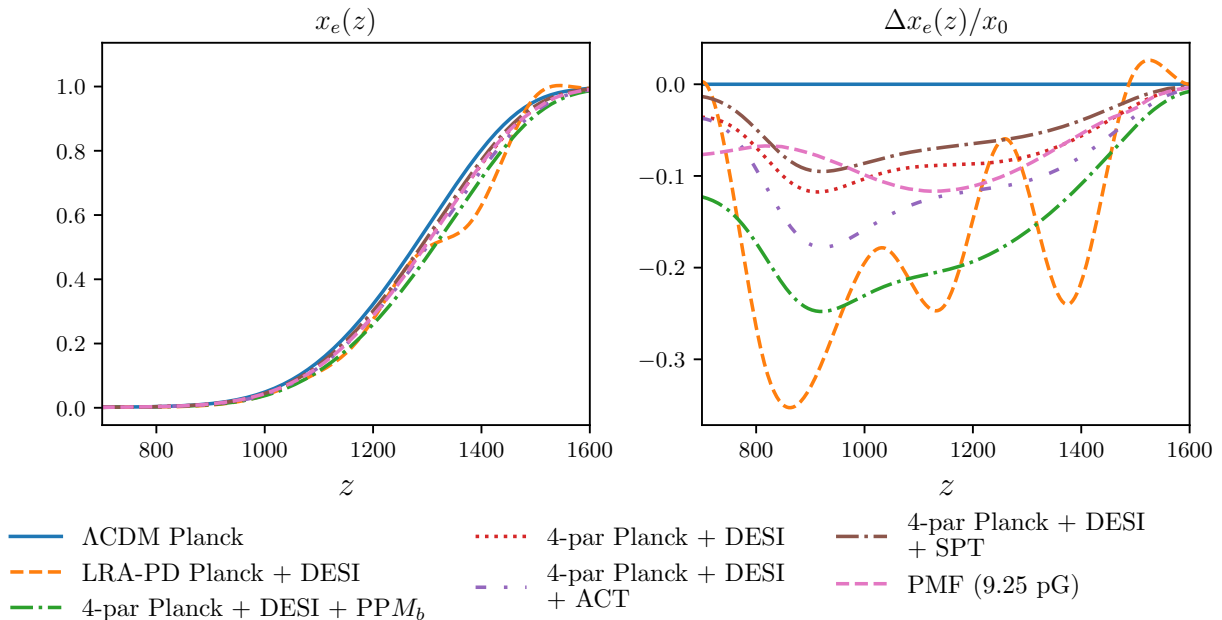


FIG. 2: The ionization histories $x_e(z)$ predicted by the LRA based on the best fit to Planck+DESI (orange dash) and the 4-parameter model best fits to Planck+DESI (red dot), Planck+DESI+ PPM_b (green dash-dot), Planck+DESI+ACT (purple dash-double-dot) and Planck+DESI+SPT (brown dash-dot). The Planck best fit Λ CDM ionization history is shown with a solid blue line. For comparison, the pink dashed line shows the $x_e(z)$ predicted by PMF of $B_{\text{rms}} = 9.25$ pG that gives a good fit to the combination of Planck and DESI.

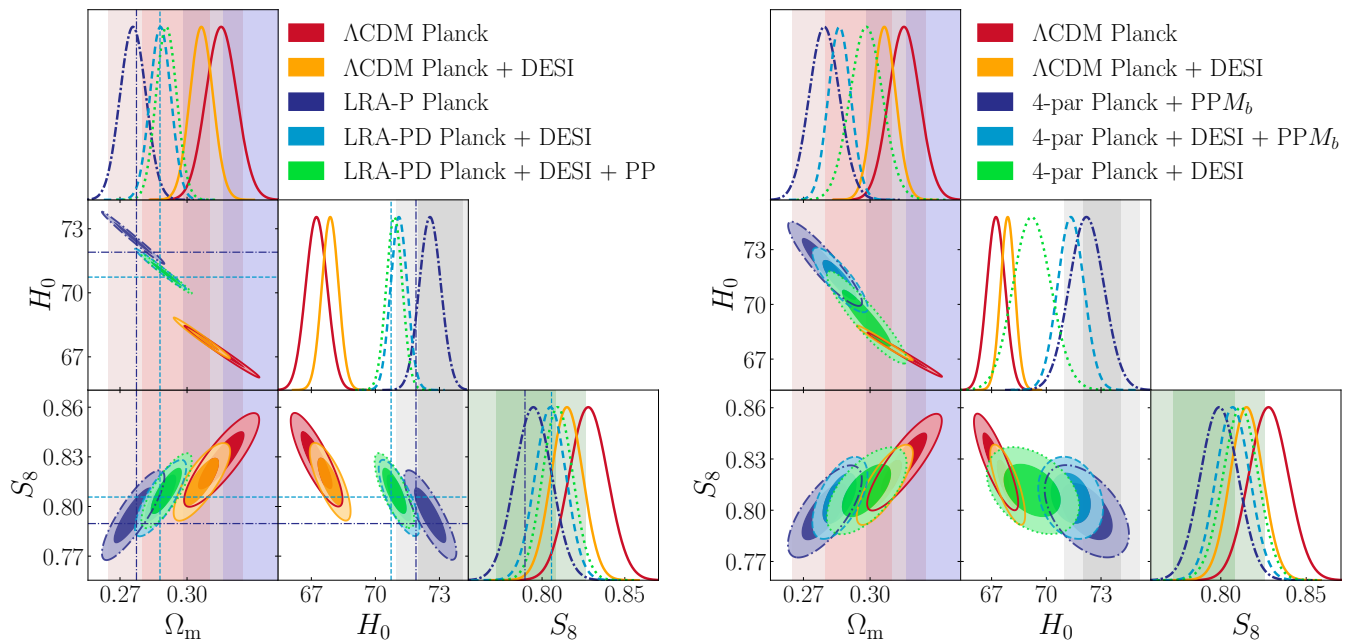


FIG. 3: The 68% and 95% CL contours of the Ω_m , H_0 , and S_8 posterior distributions for the LRA-P and LRA-PD models (left) and the 4-parameter model (right) fit to combinations of Planck, DESI, PP and PPM_b as discussed in the text. For reference, the red, blue, grey and green vertical bands show the 68% and 95% CL intervals for $\Omega_m = 0.295 \pm 0.015$ from DESI, $\Omega_m = 0.334 \pm 0.018$ from PP, $H_0 = 73.04 \pm 1.04$ from SH0ES, and $S_8 = 0.790^{+0.018}_{-0.014}$ from DES-Y3 + KIDS-1000 respectively. The dark(light) blue dash-dotted (dashed) lines show the best fit values predicted by the LRA method for Planck (Planck+DESI).

bination of Planck and DESI that predicts $H_0 = 70.74$ km/s/Mpc, $S_8 = 0.806$, and $\Delta\chi_{\text{BF}}^2 = -4.77$. We will treat these two ionization histories as two specific models of modified recombination, labeled as “LRA-P” and “LRA-PD”, that we will fit to the data alongside the Λ CDM and the 4-parameter model. We do this in order to test the accuracy of the LRA prediction, examine the importance of the wiggles in $x_e(z)$, and investigate the impact of adding other datasets, such as ACT, SPT, PP and PPM_b . The LRA-PD $x_e(z)$ is shown in Fig. 2.

Fig. 3 shows the marginalized posteriors for Ω_m , S_8 and H_0 obtained from the MCMC fits of the LRA-P and LRA-PD models, and the 4-parameter model, to several data combinations. The mean values and 68% confidence level (CL) uncertainties in these and other relevant parameters, along with the Planck and DESI BAO best fit χ^2 are provided in Table I. In the case of the two LRA models, the LRA predicted values of these three parameters are shown with dash-dotted (dashed) vertical and horizontal lines in the left panel of Fig. 3. The posteriors of the LRA-P model parameters fit to Planck show that the reduction in the H_0 and S_8 tensions is not as good as predicted by the LRA, but still considerable. We find $H_0 = 72.57 \pm 0.47$ km/s/Mpc, while reducing the Planck χ^2 by 2.92 relative to the Λ CDM fit to Planck. This model also predicts $\Omega_m = 0.2758 \pm 0.0054$, which is in a 3.1σ tension with PP. The LRA-PD model fit to the combination of Planck and DESI also does not reduce the tensions as well as predicted by the LRA, but still shows a significant reduction of it with $H_0 = 71.09 \pm 0.37$ km/s/Mpc, while improving both the Planck and the DESI χ^2 . It also yields $\Omega_m = 0.2882 \pm 0.0045$ that is in a 2.5σ tension with PP. In both LRA models, the value of S_8 is lower than in the corresponding Λ CDM model. The impact of adding the PP dataset to the fit of the LRA-PD model is relatively minor, as shown in Fig. 3, slightly shifting Ω_m to a higher value and correspondingly lowering H_0 and increasing S_8 . We note that the smallness of the cosmological parameter uncertainties in the LRA model fits is due to the fact that it has no additional free parameters – the relative change in $x_e(z)$ is fixed.

The right panel of Fig. 3 shows the H_0 , S_8 and Ω_m posteriors from the 4-parameter model fits to Planck+DESI, Planck+ PPM_b and Planck+DESI+ PPM_b . The addition of the PPM_b dataset plays the role of “the SH0ES prior”, directing the fit towards ionization histories that yield larger values of H_0 . To assess the goodness of these fits, Table I compares the Planck and the DESI χ^2 to those the Λ CDM model. As one can see from Fig. 3 and Table I, a simple model of $x_e(z)$ can in fact relieve the H_0 tension while improving the CMB and BAO fits. When fit to Planck+DESI (without “the SH0ES prior”), it reduces the H_0 tension to 2.7σ while improving χ_{Planck}^2 by 3.3 and χ_{BAO}^2 by 2.8, a reduction in the total χ^2 by 6.1 after adding 4 parameters. When fit to Planck+ PPM_b and Planck+DESI+ PPM_b , the 4-parameter model yields H_0 values very similar to those from the corresponding LRA

models.

The $x_e(z)$ corresponding to the Planck+DESI and Planck+DESI+ PPM_b best-fit 4-parameter models are shown in Fig. 2 with the means and the 68% CL uncertainties of the parameters dz_{sh} , A_b , z_b and σ_b given in Table I. In addition to the expected $dz_{\text{sh}} < 0$ favouring earlier recombination, the $x_e(z)$ in these models feature a dip in the $800 \lesssim z \lesssim 1100$ range, with a minimum around $z \approx 930$. One can see that the Planck+DESI+ PPM_b best-fit 4-parameter model $x_e(z)$ is broadly consistent with that of LRA-PD after smoothing over the wiggles.

Based on the above results, one can conclude that the presence of wiggles in $x_e(z)$ is not essential for relieving the Hubble tension. To make this statement more concrete, we compare the goodness of the fits more systematically in Table III of Appendix B, where the differences in best fit χ^2 are based on fits to identical data combinations (relative to the corresponding Λ CDM fit). Whereas the wiggly LRA model ionization histories perform somewhat better when fit to Planck + PPM_b , the same does not hold true when the DESI data is added.

A. Implications for the high- ℓ CMB spectra

As discussed in Sec. II, modified recombination relieves the Hubble tension by increasing z_* , shifting the peak of the visibility function to an earlier epoch. However, changes to the shape of the visibility function that accompany such a shift are also very important, as they affect the amplitude of the E-mode polarization [47] and the suppression of CMB anisotropies in the Silk damping tail [48] at $\ell > 1500$. The high- ℓ anisotropy spectra, therefore, provide a critical test of these models in light of the high-resolution CMB experiments that are already placing non-trivial constraints on modified recombination [24, 48], and with more stringent tests expected with the data from the Simons Observatory [49] and CMB-S4 [50].

Fig. 4 shows the visibility functions $g(z)$ corresponding to the best-fit recombination models discussed earlier. We see that the shifts in the peak are accompanied by different degree of broadening of the visibility function¹. Notably, the LRA-PD model has a broader $g(z)$, while the two 4-parameter models have $g(z)$ comparable or slightly narrower than of the Λ CDM model.

The corresponding relative differences in the CMB spectra at high ℓ are plotted in Fig. 5 along with the ACT DR [46] and SPT-3G [45] data. Interestingly, the LRA-PD model, which has the wider visibility function and wiggly $x_e(z)$, shows the larger differences with respect to Λ CDM at higher ℓ , while the two 4-parameter model spectra are generally close to those in Λ CDM.

¹ The visibility function is normalized to unity, so a lower peak indicates a broader function.

Parameter	Λ CDM	LRA-P	4-par Planck	Λ CDM	LRA-PD	4-par Planck	4-par Planck
	Planck	Planck	+ PPM _b	Planck + DESI	Planck + DESI	+ DESI	+ DESI + PPM _b
H_0 [km/s/Mpc]	67.24 ± 0.47	72.57 ± 0.47	72.21 ± 0.89	67.88 ± 0.37	71.09 ± 0.37	69.23 ± 0.98	71.34 ± 0.68
H_0 tension	5.08σ	0.41σ	0.61σ	4.67σ	1.77σ	2.67σ	1.37σ
S_8	0.828 ± 0.011	0.795 ± 0.010	0.799 ± 0.010	0.815 ± 0.009	0.805 ± 0.009	0.812 ± 0.010	0.807 ± 0.009
S_8 tension	1.80σ	0.24σ	0.44σ	1.24σ	0.75σ	1.07σ	0.84σ
Ω_m	0.315 ± 0.006	0.276 ± 0.005	0.279 ± 0.006	0.306 ± 0.005	0.288 ± 0.004	0.298 ± 0.007	0.286 ± 0.005
Ω_m tension	0.97σ	3.10σ	2.85σ	1.47σ	2.47σ	1.85σ	2.56σ
$\Omega_m h^2$	0.143 ± 0.001	0.145 ± 0.001	0.146 ± 0.001	0.141 ± 0.001	0.146 ± 0.001	0.143 ± 0.002	0.146 ± 0.001
$100 \Omega_b h^2$	2.219 ± 0.013	2.283 ± 0.013	2.274 ± 0.017	2.229 ± 0.013	2.248 ± 0.012	2.246 ± 0.018	2.266 ± 0.016
A_b	—	—	0.32 ± 0.10	—	—	< 0.219	$0.30^{+0.10}_{-0.12}$
z_b	—	—	936 ± 22	—	—	911^{+70}_{-21}	928 ± 22
σ_b	—	—	153^{+30}_{-20}	—	—	< 194	163^{+30}_{-20}
dz_{sh}	—	—	$-43.1^{+7.6}_{-9.8}$	—	—	$-19.5^{+13}_{-9.9}$	$-39.1^{+7.7}_{-8.8}$
χ^2_{Planck}	10972.82	10969.90	10972.82	10974.08	10973.50	10970.79	10972.87
χ^2_{BAO}	—	—	—	15.67	14.03	12.91	14.96

TABLE I: The mean values and the 68% uncertainties for parameters of special interest from the MCMC runs represented in Fig. 3, along with the best-fit Planck and DESI chi-squared values.

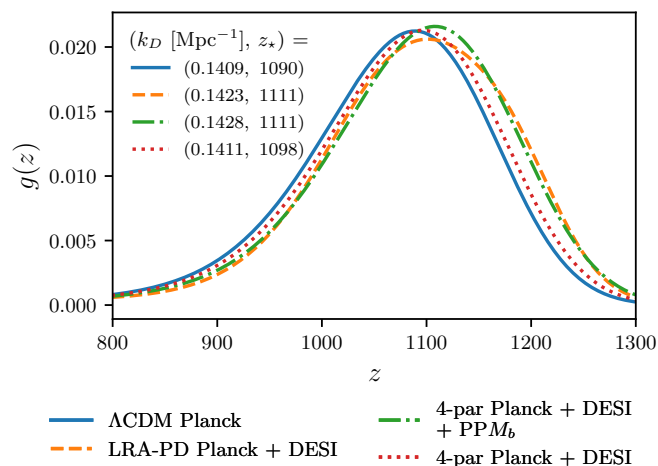


FIG. 4: The visibility functions $g(z)$ for the Planck+DESI best-fit LRA-PD model, the Planck+DESI and Planck+DESI+PPM_b best-fit 4-parameter models, and the Λ CDM model. The legend lists the corresponding values of the Silk damping wavenumber k_D and the redshift of the peak of the visibility function z_* .

We note that our LRA-PD CMB residuals are similar to those shown in Fig. 14 of Lynch *et al* [27]. When fitting the LRA+PD model to Planck+DESI+ACT and Planck+DESI+SPT, we see a substantial increase in the ACT and the SPT χ^2 compared to the corresponding Λ CDM fits, with the corresponding numbers provided in Tables IV and V of Appendix B. One should keep in mind that the LRA-PD model was not optimized to fit ACT or SPT, so such an outcome is not surprising. Nevertheless, it demonstrates how a model that provides a very good fit to Planck+DESI, while reducing the Hubble tension,

Name	4-par PL +DESI	4-par PL +DESI +ACT	4-par PL +DESI +SPT
H_0	69.23 ± 0.98	69.90 ± 0.91	69.11 ± 0.91
S_8	0.812 ± 0.010	0.812 ± 0.009	0.811 ± 0.010
Ω_m	0.298 ± 0.007	0.295 ± 0.006	0.299 ± 0.007
$\Delta\chi^2_{\text{PL}}$	-3.28	-5.34	-1.50
$\Delta\chi^2_{\text{BAO}}$	-2.76	-1.25	-2.89
$\Delta\chi^2_{\text{PL+BAO}}$	-6.04	-6.59	-4.39
$\Delta\chi^2_{\text{ACT}}$	—	-0.26	—
$\Delta\chi^2_{\text{SPT}}$	—	—	+2.92
$\Delta\chi^2_{\text{total}}$	-6.04	-6.85	-1.47

TABLE II: The mean values and the 68% uncertainties for parameters of special interest along with the change in best-fit χ^2 values relative the corresponding Λ CDM best fits for the 4-parameter model fit to the combinations of Planck (denoted as PL), DESI, ACT and SPT.

can be strongly constrained even by the current high- ℓ anisotropy data.

As mention above, the high- ℓ anisotropy spectra are very sensitive not only to the peak but also to the shape of the visibility function. The spectra are affected by the combination of factors that include the Silk damping scale, which is generally smaller for earlier recombination, the amplitude of the E-mode polarization, which is generally larger for broader $g(z)$ [47], the optical depth τ , the overall amplitude A_s and the spectral index n_s . Our limited analysis in Sec. IV A does not point to a single dominant factor explaining the large difference in the residuals between the LRA-PD and the 4-parameter model residuals, although it is expected that the param-

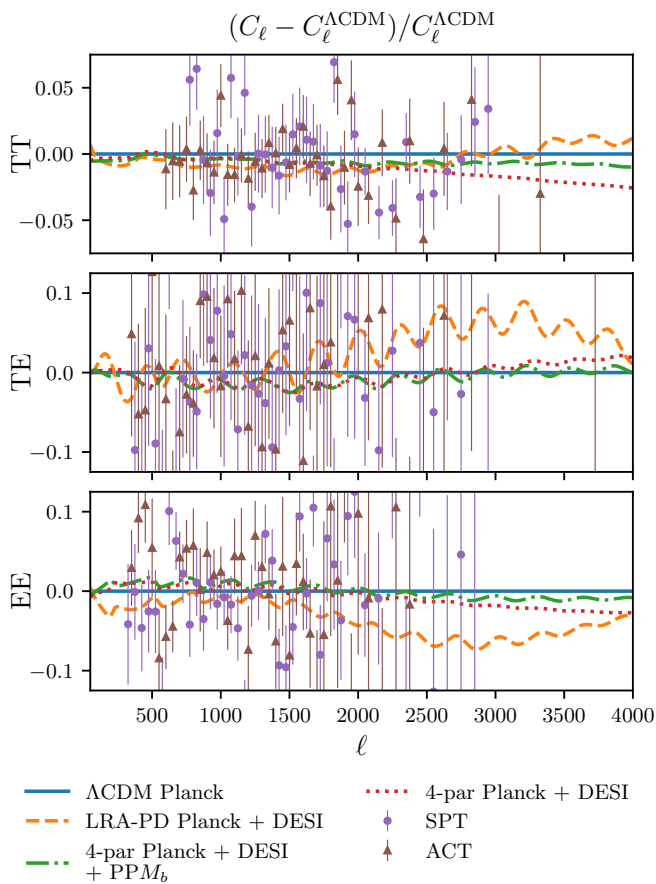


FIG. 5: Relative differences in the CMB spectra with respect to the Planck best-fit Λ CDM model for the Planck+DESI best-fit LRA-PD model, and the Planck+DESI+PPM_b and Planck+DESI best-fit 4-parameter models. Also shown are the 2022 SPT-3G and ACT DR4 minimum-variance band power errors. In the case of TE, to avoid divisions by zero, we plot $(C_\ell^{\text{TE}} - C_\ell^{\text{TE},\Lambda\text{CDM}})/C_\ell^{\text{ref}}$, where C_ℓ^{ref} is the absolute value of $C_\ell^{\text{TE},\Lambda\text{CDM}}$ convolved with a Gaussian of width $\sigma_\ell = 100$ centred at ℓ .

eter adjustments required to compensate for the notably broader $g(z)$ (which affects polarization differently from temperature anisotropies) in order to preserve the good fit to Planck, would yield larger differences at high ℓ .

We also fit the 4-parameter model to Planck+DESI+ACT and Planck+DESI+SPT to see how adding the high- ℓ datasets affects the ability of simple recombination models to resolve the Hubble tension. We perform these fits without the PPM_b dataset, *i.e.* without the SH0ES prior. We find that, compared to fitting the 4-parameter model to Planck+DESI, adding the ACT data yields a higher mean value of H_0 , and further reducing the χ^2 for all CMB datasets relative to the corresponding Λ CDM models, as shown in Table II (see also Table VI of Appendix B). On the other hand, adding the SPT data has the opposite effect, reducing the mean value of H_0 and increasing the χ^2 values. This, again, demonstrates how important

the future high- ℓ CMB anisotropy spectra will be for discriminating between modified recombination models.

V. DISCUSSION

The results presented in the previous Section are consistent with previous studies of modified recombination [26–28] and the general expectations for all models that attempt to relieve the Hubble tension by reducing the sound horizon. In particular, we have shown that it is possible to find ionization histories that increase the CMB-inferred value of H_0 to greater than 72 km/s/Mpc, eliminating the tension between Planck and SH0ES. The existence of this possibility is not trivial as the successful models have to preserve the good fit to the fine features of the CMB TT, TE and EE spectra [14]. We found that the more flexible models of the ionization history based on cubic-splines that allow for wiggly $x_e(z)$ were somewhat more successful in achieving high values of H_0 than the simple 4-parameter model when fit to the Planck data alone.

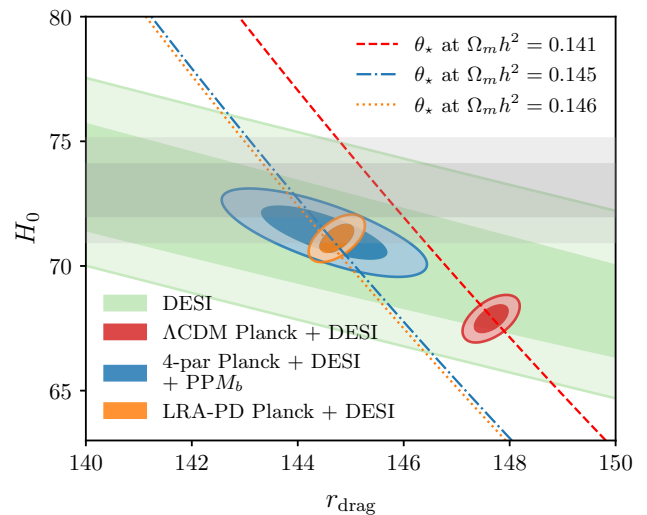


FIG. 6: The 68% and 95% CL bands of r_{drag} , H_0 derived from DESI BAO data marginalized over $\omega_m \equiv \Omega_m h^2$ (pale green), from the LRA-PD model (orange) fit to Planck+DESI, the 4-parameter model (blue) fit to Planck+DESI+PPM_b and the Λ CDM model fit to Planck+DESI (red). Also shown are the $r_{\text{drag}}-H_0$ degeneracy lines defined by the CMB acoustic scale θ_* at the $\Omega_m h^2$ values corresponding to the best-fit values for each model. The grey band shows the 68% and 95% CL determination of the Hubble constant by SH0ES.

Fully solving the Hubble tension while preserving a good fit to the combination of CMB and BAO is more challenging for the general reasons presented in [30] and which we briefly outline here. For a given value of $\Omega_m h^2$, the observed CMB acoustic scale θ_* defines a line in the $r_{\text{drag}}-H_0$ plane. Fig. 6 shows three such lines at three different values of $\Omega_m h^2$ corresponding to the

best-fit Λ CDM, the best-fit LRA Planck+DESI and the Planck+DESI+PPM_b best fit 4-parameter model, as well as the 68% and 95% CL bands from DESI BAO after marginalizing over $\Omega_m h^2$, and the H_0 measurement by SH0ES. One can see that raising H_0 to values above 71 km/s/Mpc by reducing r_{drag} is challenging, as it would require a much larger value of $\Omega_m h^2$ in order for the θ_* line to pass through the region where the DESI and SH0ES bands overlap. Such large values of $\Omega_m h^2$ would not be compatible with CMB in modified $x_e(z)$ models, and would worsen the S_8 tension [30].

With $H_0 > 71$ km/s/Mpc ruled out by the necessity to simultaneously accommodate the acoustic scales measured by both CMB and BAO, the need for the wiggly shape of $x_e(z)$ goes away. Our results suggest that the presence of wiggles in $x_e(z)$ could be helpful for achieving a Planck-best-fit value of $H_0 > 72$ km/s/Mpc, but it was not essential for getting $H_0 \sim 71$ km/s/Mpc. We also found that the Planck+DESI and Planck+DESI+PPM_b best fit 4-parameter models had substantially smaller high- ℓ residuals relative to the Planck best-fit Λ CDM.

For reference, Fig. 2 also shows the ionization history obtained from magnetohydrodynamic (MHD) simulations of the primordial plasma through the epoch of recombination in the presence of PMF. The baryon clumping induced by PMF speeds up recombination and helps relieve the Hubble tension [23]. The $x_e(z)$ shown in Fig. 2 is for a PMF with a blue Batchelor spectrum (predicted for PMF generated in phase transitions) and a root-mean-square post-recombination comoving strength of $B_{\text{rms}} = 9.25$ pG, and is based on recent MHD simulations that take into account all relevant effects, such as the Lyman- α photon transport across regions of higher and lower density [37]. It is intriguing that this $x_e(z)$, which provides a good fit to the combination of Planck and DESI, has a shape that is not too far from the ionization histories of the best fit 4-parameter models. This is particularly nontrivial given the very low success rate when searching for viable modified ionization histories using the LRA method, as mentioned at the beginning of Sec IV.

The S_8 tensions is trivially reduced in models of modified recombination that yield larger values of H_0 . This is because $\Omega_m h^2$ does not change by much in these models, and neither do the other cosmological parameters that determine σ_8 . Hence, a larger h automatically implies a smaller Ω_m and hence a smaller S_8 ($S_8 \equiv \sigma_8 \sqrt{\Omega_m/0.3}$).

The fact that modified recombination solutions to the Hubble tension generically reduce Ω_m exacerbates the disagreement with the larger Ω_m measured from the recent SN datasets, as also pointed out in [22, 26]. However, for the models we studied, this tension is in the 2-3 σ range (see Table I), which is relatively mild. Furthermore, there are good reason for viewing the Ω_m problem as being separate from the Hubble tension. It arises from the fact that the shapes of the conformal distance-redshift curves deduced from the uncalibrated BAO and SN datasets covering the same redshift range are not

well-accommodated by the same flat Λ CDM cosmology – DESI BAO measure $\Omega_m = 0.295 \pm 0.015$ [9], while PP SN yield $\Omega_m = 0.334 \pm 0.018$ [6]. Departures from the flat Λ CDM, such as the dynamical dark energy models which fit the BAO+SN combination better, do not help raise the value of H_0 [9]. We also note that Planck and DESI are in excellent consistency with each other in models with lower sound horizon that yield $H_0 \sim 70$ km/s/Mpc [29].

VI. SUMMARY

Our study demonstrated that it is possible to reduce the Hubble tension below 2σ by modifying the ionization history $x_e(z)$, while preserving and even improving the fit to the current CMB and BAO data and reducing the S_8 tension. We considered two models of $x_e(z)$: a fully agnostic parameterization using a cubic-spline through 7 nodes in redshift, and a phenomenological 4-parameter model motivated by the ionization histories derived from simulations of recombination in the presence of PMF. While the cubic-spline parameterization yields wiggly best-fit shapes of $x_e(z)$, our analysis showed that the presence of wiggles is not essential for achieving good fits to the combination of CMB and BAO data with $H_0 \sim 71$ km/s/Mpc. Our study also confirmed that the high-resolution CMB temperature and polarization anisotropies measured by ACT, SPT, Simons Observatory [49] and CMB-S4 [50] have a crucial role in discriminating between models of modified recombination. Overall, modifying recombination remains a viable option for resolving the Hubble tension.

Acknowledgments

We thank Jens Chluba, Gabriel Lynch, Ali Nezhad-safavi and Xavier Wang for useful discussions. This research was enabled in part by support provided by the BC DRI Group and the Digital Research Alliance of Canada (alliancecan.ca). S.H.M and L.P. are supported in part by the National Sciences and Engineering Research Council (NSERC) of Canada.

Appendix A: Details of the LRA analysis

In this section, we provide additional details related to the LRA analysis, where we closely followed the methods used in [26].

1. Calculating the shifts in the best-fit parameters

Assuming the modified recombination model is sufficiently close to the fiducial Λ CDM cosmology, one can

compute the change in the observable \mathbf{X} due to a perturbation of the ionization history $\Delta \ln [x_e(z)]$ as

$$\Delta \mathbf{X} = \int dz \frac{\delta \mathbf{X}}{\delta \ln [x_e(z)]} \Delta \ln [x_e(z)]. \quad (\text{A1})$$

The best-fit parameters and chi-squared of the modified model will be different from those of the fiducial model. The shifts in the best-fit parameters and chi-squared due to a perturbation $\Delta \ln [x_e(z)]$ can be written as

$$\Delta \Omega_{\text{BF}}^i = \int dz \frac{\delta \Omega_{\text{BF}}^i}{\delta \ln [x_e(z)]} \Delta \ln [x_e(z)], \quad (\text{A2a})$$

$$\begin{aligned} \Delta \chi_{\text{BF}}^2 &= \int dz \frac{\delta \chi_{\text{BF}}^2}{\delta \ln [x_e(z)]} \Delta \ln [x_e(z)] \\ &+ \frac{1}{2} \iint dz dz' \frac{\delta^2 \chi_{\text{BF}}^2}{\delta \ln [x_e(z)] \delta \ln [x_e(z')]} \Delta \ln [x_e(z)] \Delta \ln [x_e(z')], \end{aligned} \quad (\text{A2b})$$

where

$$\frac{\delta \Omega_{\text{BF}}^i}{\delta \ln [x_e(z)]} = -(F^{-1})_{ij} \frac{\partial \mathbf{X}}{\partial \Omega^j} \cdot \mathbf{M} \cdot \frac{\delta \mathbf{X}}{\delta \ln [x_e(z)]}, \quad (\text{A3a})$$

$$\frac{\delta \chi_{\text{BF}}^2}{\delta \ln [x_e(z)]} = 2[\mathbf{X}(\vec{\Omega}_{\text{fid}}) - \mathbf{X}^{\text{obs}}] \cdot \widetilde{\mathbf{M}} \cdot \frac{\delta \mathbf{X}}{\delta \ln [x_e(z)]}, \quad (\text{A3b})$$

$$\frac{\delta^2 \chi_{\text{BF}}^2}{\delta \ln [x_e(z)] \delta \ln [x_e(z')]} = 2 \frac{\delta \mathbf{X}}{\delta \ln [x_e(z)]} \cdot \widetilde{\mathbf{M}} \cdot \frac{\delta \mathbf{X}}{\delta \ln [x_e(z')]}, \quad (\text{A3c})$$

where F_{ij} , \mathbf{M} , $\widetilde{\mathbf{M}}$, and $\delta \mathbf{X} / \delta \ln [x_e(z)]$ are all to be evaluated at the fiducial cosmology and in the standard model. Here, $\widetilde{\mathbf{M}}$ is defined as

$$\widetilde{M}_{\alpha\beta} \equiv M_{\alpha\beta} - M_{\alpha\gamma} \frac{\partial X^\gamma}{\partial \Omega^i} (F^{-1})_{ij} \frac{\partial X^\sigma}{\partial \Omega^j} M_{\sigma\beta}, \quad (\text{A4})$$

and it can be interpreted as the inverse of the covariance matrix after marginalization over shifts in standard cosmological parameters [26].

2. Evaluating functional derivatives

We build an orthonormal set of response functions to form a vector space that generates perturbations in $x_e(z)$ over given narrow redshift ranges. We define Gaussian shapes used for the principal component analysis in [32], since they are smooth and easy to implement into the Boltzmann equation solver². The generated basis func-

² Strictly speaking, Gaussian functions are not orthogonal to each other, but for all practical purposes, they are when hardly overlapping.

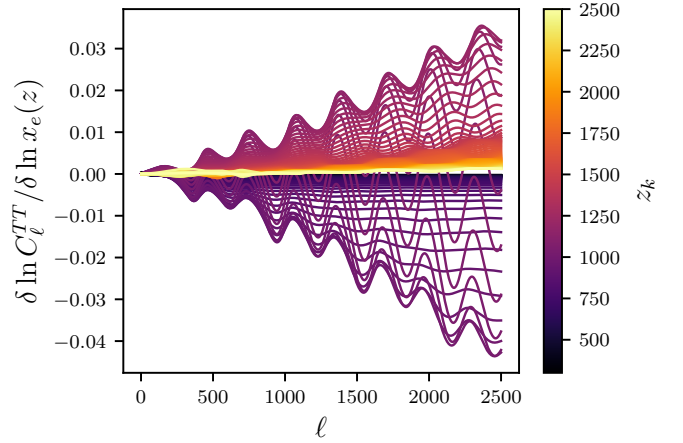


FIG. 7: Derivatives of the CMB temperature power spectrum with respect to the ionized fraction using the basis functions in (A5), with the pivot redshifts z_k spanning the range $[z_{\min}, z_{\max}] = [300, 2500]$.

tions are given by

$$\begin{aligned} \Delta \ln [x_e(z, z_k)] &\equiv \frac{\Delta x_e}{x_0}(z, z_k) \\ &= \frac{1}{\sqrt{2\pi\sigma^2}} \exp\left[-\frac{(z - z_k)^2}{2\sigma^2}\right], \quad \sigma \equiv \frac{z_{\max} - z_{\min}}{6N\sqrt{2\ln 2}}. \end{aligned} \quad (\text{A5})$$

Here, z_{\min} and z_{\max} define the boundaries of the redshift range, while N represents the number of basis functions, each associated with a pivot redshift z_k within that range. We generate $N = 121$ basis functions in the redshift range of $[z_{\min}, z_{\max}] = [300, 2500]$. This selection of N guarantees the convergence of sampled components, being large enough to remove all non-orthogonalities, yet not too large to cause highly non-linear responses where obtained functions are no longer smooth. The selected redshift range covers the epoch of hydrogen and helium recombination. Outside this range, the CMB anisotropies vary negligibly unless we move into the reionization era at $z \leq 10$.

We implement the basis functions via RECFAST into the Boltzmann solver code CAMB, and analyze the response of the CMB anisotropy power spectra, and BAO measurements. The functional derivatives of the observables at each pivot redshift z_k are calculated via numerical differentiation by using three-point midpoint formula:

$$\begin{aligned} \frac{\delta \mathbf{X}}{\delta \ln x_e(z)} &\equiv \frac{\delta \mathbf{X}}{\delta x_e(z)/x_0} \\ &= \frac{\mathbf{X}[x_0 + \Delta x_e(z, z_k)] - \mathbf{X}[x_0 - \Delta x_e(z, z_k)]}{2\Delta x_e(z, z_k)/x_0} \Bigg|_{z=z_k}. \end{aligned} \quad (\text{A6})$$

The changes in the ionization history affect CMB anisotropies via the Thomson visibility function. Fig. 7 shows the derivative of the logarithm of the temperature

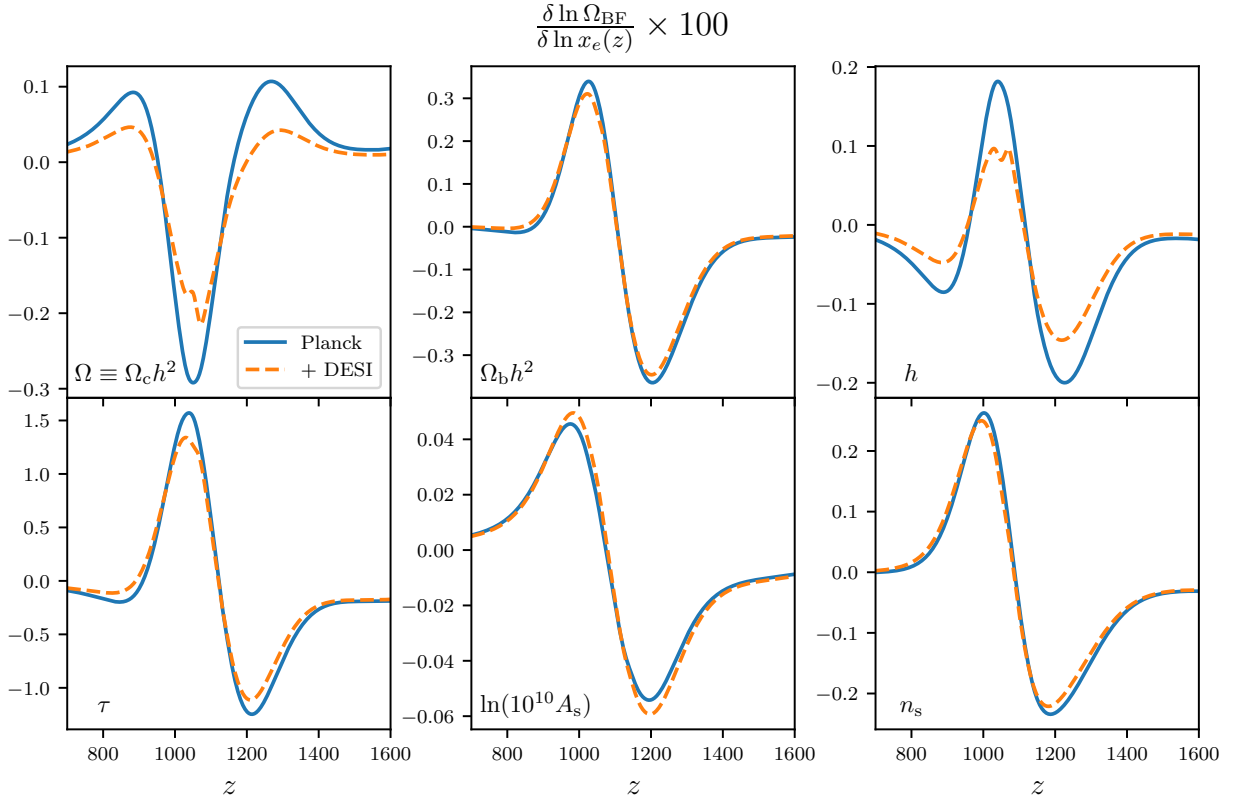


FIG. 8: Functional derivatives of the best-fit cosmological parameters for Planck and Planck+DESI data. The plots cover the redshift range of $z = [700, 1600]$. The CMB data shows little sensitivity to perturbations in $x_e(z)$ outside this range.

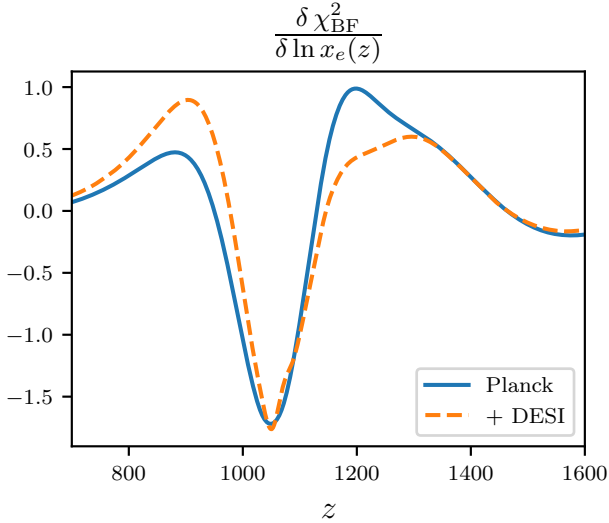


FIG. 9: The functional derivatives of the best-fit chi-squared for Planck and Planck+DESI data.

power spectrum with respect to logarithm of x_e at redshifts z_k . The strongest response occurs around the peak of the visibility function ($z_* \simeq 1100$) with about 4% maximum amplitude. The colour bar shows that the change in the slopes of spectra is positive for $z > z_*$, and a neg-

ative response for $z < z_*$. The precise calculation of the functional derivatives requires a boost in the `CAMB` accuracy parameters. In particular, we reduced the time step by a factor of 20, as one needs a high resolution time-sampling around recombination to avoid discontinuities in the Boltzmann equation solver, achieving numerically-stable responses.

With the derivatives of the observables at hand, we use (A3) to calculate the functional derivatives of the cosmological parameters and chi-squared, which are then used to find the shifts in the best-fit values. Figures 8, 9 and 10 illustrate these derivatives, showing the changes in the best-fit cosmological parameters, best-fit chi-squared, and the quadratic response of the best-fit chi-squared $\delta^2 \chi_{\text{BF}}^2 / \delta \ln[x_e(z)] \delta \ln[x_e(z')]$ with respect to variations in $\ln[x_e(z)]$.

3. Generating trial recombination histories $\Delta \ln[x_e(z)]$

We parameterize $\Delta \ln[x_e(z)] = \Delta x_e(z)/x_0$ using a cubic spline passing through 7 control points placed evenly between $z_a = 700$ and $z_b = 1600$. We set $\Delta x_e = 0$ outside this range, as the CMB data show negligible sensitivity to the changes in ionization history beyond these redshifts, as illustrated in Fig. 8. The departures from

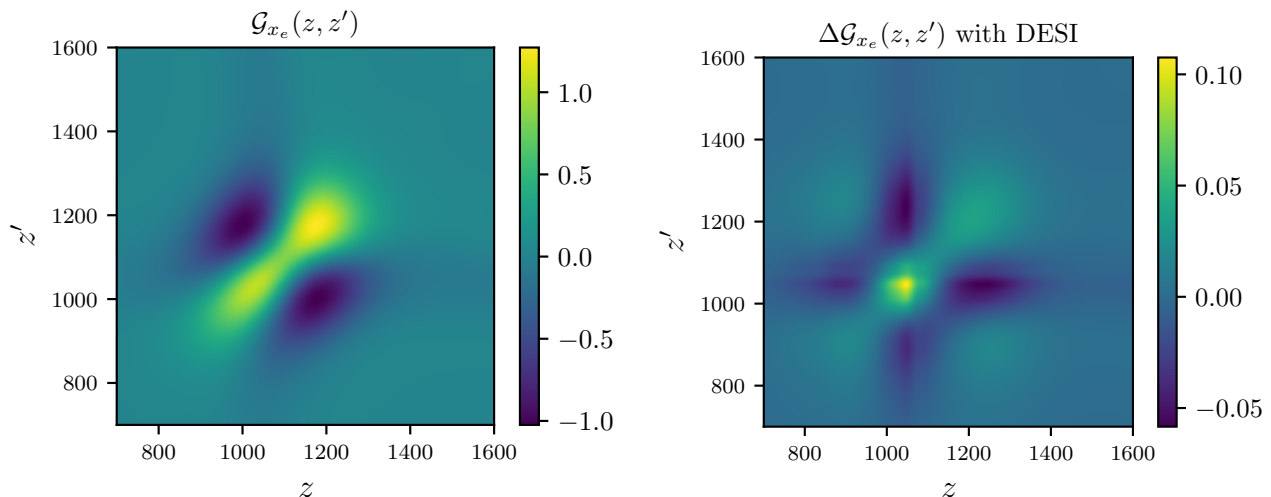


FIG. 10: The quadratic response of the best-fit chi-squared $\mathcal{G}_{x_e}(z, z') \equiv \delta^2 \chi_{\text{BF}}^2 / \delta \ln[x_e(z)] \delta \ln[x_e(z')]$ with respect to logarithmic variations in $x_e(z)$ at each redshift for the Planck data (left) and DESI BAO data (right).

standard recombination at each control point are chosen from 6 amplitudes uniformly spaced between 0 and dx_{max} . This configuration provides us with the possibility of generating a large number (i.e. $6^7 \approx 280000$) of recombination histories to investigate deviations from the standard recombination. We also tried four different values of dx_{max} , $(-0.2, -0.25, -0.3, -0.35)$. We developed a Python pipeline to identify candidate splines that

meet our criteria of $H_0^{\text{BF}} \geq 70$, $\Delta \chi_{\text{BF}}^2 \leq 0$. Using a modified version of CAMB that takes the generated cubic splines and the corresponding best-fit cosmological parameters from the Python code as input, we calculate the derived value of S_8 parameter. This allows us to apply our third criterion, $S_8^{\text{BF}}(\Delta \ln[x_e(z)]) < S_8^{\text{fid}}$, to filter out the remaining ineligible splines.

Appendix B: Parameter tables

$\Delta \chi_{\text{BF}}^2$	LRA-P Planck	LRA-PD Planck + DESI	LRA-P Planck + PPM_b	LRA-PD Planck + DESI + PPM_b	4-par Planck +DESI	4-par Planck + PPM_b	4-par Planck + DESI + PPM_b
low- ℓ TT	+0.36	+3.68	+1.67	+3.44	+0.10	+1.61	+0.37
low- ℓ EE	+0.05	-0.08	-0.68	-1.15	-0.10	-0.82	-1.18
high- ℓ	-4.74	-4.07	-9.78	-5.69	-2.96	-6.08	-3.21
lensing	+1.41	-0.10	-0.69	-0.14	-0.33	-1.02	-0.51
$\Delta \chi_{\text{CMB}}^2$	-2.92	-0.58	-9.49	-3.55	-3.29	-6.30	-4.53
$\Delta \chi_{\text{BAO}}^2$	-	-1.64	-	+0.53	-2.76	-	+1.42
$\Delta \chi_{\text{SN}}^2$	-	-	+4.33	+2.85	-	+5.06	+3.90
$\Delta \chi_{\text{SHOES}}^2$	-	-	-29.61	-26.03	-	-30.41	-27.97
$\Delta \chi_{\text{total}}^2$	-2.92	-2.22	-34.77	-26.20	-6.04	-31.65	-27.18

TABLE III: Changes in the best-fit chi-squared values $\Delta \chi_{\text{BF}}^2$ for the LRA-P, LRA-PD and the 4-parameter model fits relative to the Λ CDM fits to the same data combinations.

Parameter	Λ CDM Planck	Λ CDM Planck + DESI	Λ CDM Planck + DESI + ACT	Λ CDM Planck + DESI + SPT	Λ CDM Planck + DESI + PP	Λ CDM Planck + DESI + PPM _b
H_0 [km/s/Mpc]	67.24 ± 0.47	67.88 ± 0.37	67.97 ± 0.35	67.87 ± 0.35	67.77 ± 0.36	68.50 ± 0.34
H_0 tension	5.08σ	4.67σ	4.62σ	4.71σ	4.79σ	4.15σ
S_8	0.828 ± 0.011	0.815 ± 0.009	0.817 ± 0.009	0.814 ± 0.009	0.817 ± 0.009	0.804 ± 0.009
S_8 tension	1.80σ	1.24σ	1.34σ	1.19σ	1.34σ	0.70σ
Ω_m	0.315 ± 0.006	0.306 ± 0.005	0.305 ± 0.005	0.306 ± 0.005	0.308 ± 0.005	0.299 ± 0.004
Ω_m tension	0.97σ	1.47σ	1.55σ	1.47σ	1.39σ	1.90σ
$\Omega_m h^2$	0.143 ± 0.001	0.141 ± 0.001	0.141 ± 0.001	0.141 ± 0.001	0.141 ± 0.001	0.140 ± 0.001
τ_{reio}	0.052 ± 0.007	0.057 ± 0.007	0.056 ± 0.007	0.055 ± 0.007	0.056 ± 0.007	$0.062^{+0.007}_{-0.008}$
n_s	0.964 ± 0.004	0.967 ± 0.004	0.970 ± 0.003	0.967 ± 0.003	0.967 ± 0.004	0.970 ± 0.003
$\log(10^{10} A_s)$	3.037 ± 0.014	3.044 ± 0.014	3.051 ± 0.013	3.042 ± 0.013	3.043 ± 0.014	$3.052^{+0.014}_{-0.015}$
M_b	–	–	–	–	–	-19.406 ± 0.010
r_* [Mpc]	144.65 ± 0.24	144.95 ± 0.20	144.97 ± 0.20	144.94 ± 0.19	144.89 ± 0.19	145.16 ± 0.19
r_{drag} [Mpc]	147.38 ± 0.24	147.65 ± 0.21	147.67 ± 0.21	147.67 ± 0.21	147.60 ± 0.21	147.81 ± 0.21
$r_{\text{drag}} h$ [Mpc]	99.10 ± 0.81	100.23 ± 0.64	100.36 ± 0.62	100.16 ± 0.62	100.01 ± 0.60	101.26 ± 0.58
z_*	1090.14 ± 0.23	1089.89 ± 0.20	1089.88 ± 0.18	1089.90 ± 0.18	1089.94 ± 0.19	1089.61 ± 0.18
z_{drag}	1059.51 ± 0.28	1059.63 ± 0.28	1059.63 ± 0.25	1059.63 ± 0.25	1059.61 ± 0.27	1059.88 ± 0.27
$10^4 \theta_*$	104.098 ± 0.025	104.115 ± 0.024	104.127 ± 0.022	104.106 ± 0.022	104.112 ± 0.024	104.132 ± 0.023
$100 Y_P$	24.578 ± 0.006	24.582 ± 0.005	24.582 ± 0.005	24.582 ± 0.005	24.581 ± 0.005	24.588 ± 0.005
σ_8	0.808 ± 0.005	0.806 ± 0.005	0.810 ± 0.005	0.805 ± 0.005	0.807 ± 0.006	0.806 ± 0.006
$\chi^2_{\text{low-}\ell \text{ TT}}$	23.80	22.74	22.16	22.55	23.48	22.83
$\chi^2_{\text{low-}\ell \text{ EE}}$	395.85	396.52	397.45	395.90	396.84	396.82
$\chi^2_{\text{high-}\ell}$	10544.46	10545.91	10549.43	10549.55	10544.97	10548.23
χ^2_{lensing}	8.71	8.91	8.37	9.24	8.76	9.53
χ^2_{Planck}	10972.82	10974.08	10977.41	10977.24	10974.05	10977.41
χ^2_{BAO}	–	15.67	14.34	16.59	16.22	13.54
χ^2_{SN}	–	–	–	–	1404.68	1406.35
χ^2_{SH0ES}	–	–	–	–	–	33.99
χ^2_{ACT}	–	–	239.73	–	–	–
χ^2_{SPT}	–	–	–	1876.88	–	–
χ^2_{total}	10972.82	10989.75	11231.48	12870.70	12394.95	12431.30

TABLE IV: Mean values and the 68% CL intervals of the parameters and the χ^2_{BF} values for the Λ CDM model fit to combinations of Planck, DESI, ACT, SPT, PP, and PPM_b.

Parameter	LRA-P		LRA-PD			
	Planck	Planck + PP	Planck + DESI	Planck + DESI + ACT	Planck + DESI + SPT	Planck + DESI + PP
H_0 [km/s/Mpc]	72.57 ± 0.47	72.12 ± 0.45	71.09 ± 0.37	71.2 ± 0.36	71.14 ± 0.35	70.89 ± 0.36
H_0 tension	0.41σ	0.81σ	1.77σ	1.67σ	1.73σ	1.95σ
S_8	0.795 ± 0.010	0.8033 ± 0.0099	0.8055 ± 0.0090	0.8064 ± 0.0089	0.8035 ± 0.0086	0.8095 ± 0.0088
S_8 tension	0.24σ	0.65	0.75σ	0.82σ	0.68σ	0.97σ
Ω_m	0.2758 ± 0.0054	0.2810 ± 0.0052	0.2882 ± 0.0045	0.2870 ± 0.0043	0.2876 ± 0.0043	0.2908 ± 0.0044
Ω_m tension	3.10σ	2.83σ	2.47σ	2.54σ	2.51σ	2.33σ
$\Omega_m h^2$	0.1452 ± 0.0010	0.1461 ± 0.0010	0.1457 ± 0.0008	0.1455 ± 0.0008	0.1455 ± 0.0008	0.1461 ± 0.0008
τ_{reio}	0.0558 ± 0.0072	0.0528 ± 0.0071	0.0515 ± 0.0068	0.0501 ± 0.0067	0.0499 ± 0.0067	0.0500 ± 0.0067
n_s	0.9620 ± 0.0038	0.9597 ± 0.0038	0.9518 ± 0.0036	0.9553 ± 0.0032	0.0499 ± 0.0067	0.0500 ± 0.0067
$\log(10^{10} A_s)$	3.042 ± 0.014	3.038 ± 0.014	3.028 ± 0.013	3.034 ± 0.013	3.027 ± 0.013	3.026 ± 0.013
r_* [Mpc]	141.52 ± 0.23	141.32 ± 0.22	141.92 ± 0.20	141.97 ± 0.19	141.95 ± 0.19	141.83 ± 0.19
r_{drag} [Mpc]	144.20 ± 0.24	144.03 ± 0.23	144.74 ± 0.21	144.78 ± 0.21	144.76 ± 0.20	144.65 ± 0.20
$r_{\text{drag}} h$ [Mpc]	104.64 ± 0.81	103.87 ± 0.76	102.90 ± 0.64	103.09 ± 0.62	102.97 ± 0.61	102.54 ± 0.61
z_*	1114.69 ± 0.24	1114.89 ± 0.24	1110.99 ± 0.22	1110.96 ± 0.21	1110.95 ± 0.20	1111.08 ± 0.22
z_{drag}	1083.12 ± 0.27	1083.03 ± 0.28	1078.22 ± 0.27	1078.22 ± 0.25	1078.25 ± 0.25	1078.18 ± 0.27
$10^4 \theta_*$	104.102 ± 0.025	104.092 ± 0.024	104.112 ± 0.024	104.123 ± 0.023	104.104 ± 0.023	104.108 ± 0.024
$100 Y_P$	24.605 ± 0.0054	24.602 ± 0.0055	24.590 ± 0.0053	24.591 ± 0.0049	24.591 ± 0.0048	24.589 ± 0.0053
σ_8	0.8288 ± 0.0057	0.8300 ± 0.0057	0.8218 ± 0.0056	0.8246 ± 0.0055	0.8207 ± 0.0054	0.8222 ± 0.0056
$\chi^2_{\text{low-}\ell \text{ TT}}$	24.16	25.58	26.43	25.73	25.87	26.79
$\chi^2_{\text{low-}\ell \text{ EE}}$	395.90	395.95	396.43	395.69	395.76	395.68
$\chi^2_{\text{high-}\ell}$	10539.72	10540.80	10541.83	10545.38	10545.38	10543.12
χ^2_{lensing}	10.12	8.87	8.81	8.49	8.41	9.14
χ^2_{Planck}	10969.90	10971.20	10973.50	10975.29	10975.42	10974.73
χ^2_{BAO}	–	–	14.03	13.93	14.20	13.50
χ^2_{SN}	–	1410.41	–	–	–	1408.43
χ^2_{ACT}	–	–	–	244.51	–	–
χ^2_{SPT}	–	–	–	–	1885.08	–
χ^2_{total}	10969.90	12381.61	10987.53	11233.73	12874.70	12396.65

TABLE V: Mean values and the 68% CL intervals of the parameters and the χ^2_{BF} values for the LRA-P and LRA-PD models fit to combinations of Planck, DESI, PP, ACT, and SPT.

Parameter	4-par Planck + PPM _b	4-par Planck + DESI	4-par Planck + DESI + PPM _b	4-par Planck + DESI + ACT	4-par Planck + DESI + SPT
H_0 [km/s/Mpc]	72.21 ± 0.89	69.23 ± 0.98	71.34 ± 0.68	69.90 ± 0.91	69.11 ± 0.91
H_0 tension	0.61σ	2.67σ	1.37σ	2.27σ	2.84σ
S_8	0.799 ± 0.010	0.812 ± 0.010	0.807 ± 0.009	0.812 ± 0.009	0.811 ± 0.010
S_8 tension	0.44σ	1.07σ	0.84σ	1.09σ	1.02σ
Ω_m	0.279 ± 0.006	0.298 ± 0.007	0.286 ± 0.005	0.295 ± 0.006	0.299 ± 0.007
Ω_m tension	2.85σ	1.85σ	2.56σ	2.05σ	1.81σ
$\Omega_m h^2$	0.146 ± 0.001	0.143 ± 0.002	0.146 ± 0.001	0.144 ± 0.001	0.143 ± 0.001
τ_{reio}	0.054 ± 0.007	0.055 ± 0.007	0.052 ± 0.007	0.053 ± 0.007	0.054 ± 0.007
n_s	0.960 ± 0.007	0.965 ± 0.007	0.960 ± 0.007	0.962 ± 0.007	0.964 ± 0.007
$\log(10^{10} A_s)$	3.037 ± 0.015	3.041 ± 0.015	3.036 ± 0.015	3.042 ± 0.014	3.038 ± 0.014
M_b	-19.300 ± 0.025	–	-19.324 ± 0.020	–	–
r_* [Mpc]	141.52 ± 0.77	143.75 ± 0.93	141.84 ± 0.76	143.12 ± 0.84	143.79 ± 0.86
r_{drag} [Mpc]	144.18 ± 0.76	146.43 ± 0.93	144.50 ± 0.75	145.80 ± 0.84	146.47 ± 0.85
$r_{\text{drag}} h$ [Mpc]	104.10 ± 0.97	101.36 ± 0.96	103.08 ± 0.69	101.91 ± 0.90	101.23 ± 0.91
z_*	1114.0 ± 5.3	1097.6 ± 6.3	1110.7 ± 5.0	1102.4 ± 5.6	1097.7 ± 5.8
z_{drag}	1082.8 ± 4.9	1067.2 ± 5.8	1079.6 ± 4.5	1071.6 ± 5.2	1067.1 ± 5.3
$10^4 \theta_*$	104.131 ± 0.034	104.128 ± 0.035	104.125 ± 0.033	104.124 ± 0.029	104.110 ± 0.030
$100 Y_{\text{P}}$	24.601 ± 0.007	24.589 ± 0.007	24.598 ± 0.007	24.589 ± 0.007	24.587 ± 0.007
σ_8	0.828 ± 0.008	0.814 ± 0.008	0.826 ± 0.008	0.819 ± 0.008	0.812 ± 0.007
A_b	0.32 ± 0.10	< 0.219	$0.30^{+0.10}_{-0.12}$	< 0.278	< 0.173
z_b	936 ± 22	911^{+70}_{-21}	928 ± 22	925^{+34}_{-24}	899^{+76}_{-20}
σ_b	153^{+30}_{-20}	< 194	163^{+30}_{-20}	193 ± 40	194^{+40}_{-60}
dz_{sh}	$-43.1^{+7.6}_{-9.8}$	$-19.5^{+13}_{-9.9}$	$-39.1^{+7.7}_{-8.8}$	$-27.5^{+11}_{-9.7}$	$-18.1^{+11}_{-7.3}$
$\chi^2_{\text{low-}\ell \text{ TT}}$	23.94	22.84	23.19	23.30	23.63
$\chi^2_{\text{low-}\ell \text{ EE}}$	395.77	396.42	395.64	396.23	395.69
$\chi^2_{\text{high-}\ell}$	10544.56	10542.95	10545.02	10543.96	10547.73
χ^2_{lensing}	8.55	8.59	9.02	8.58	8.70
χ^2_{Planck}	10972.82	10970.79	10972.87	10972.07	10975.74
χ^2_{BAO}	–	12.91	14.96	13.09	13.70
χ^2_{SN}	1412.98	–	1410.25	–	–
χ^2_{SHOES}	1.71	–	6.02	–	–
χ^2_{ACT}	–	–	–	239.47	–
χ^2_{SPT}	–	–	–	–	1879.80
χ^2_{total}	12387.5	10983.70	12404.11	11224.63	12869.24

TABLE VI: Mean values and the 68% CL intervals of the parameters and the χ^2_{BF} values for the 4-parameter model fit to combinations of Planck, DESI, PPM_b, ACT, and SPT.

-
- [1] A. G. Riess et al., *Astrophys. J. Lett.* **934**, L7 (2022), 2112.04510.
- [2] A. G. Riess, L. Breuval, W. Yuan, S. Casertano, L. M. Macri, J. B. Bowers, D. Scolnic, T. Cantat-Gaudin, R. I. Anderson, and M. C. Reyes, *Astrophys. J.* **938**, 36 (2022), 2208.01045.
- [3] T. M. C. Abbott et al. (Kilo-Degree Survey, DES), *Open J. Astrophys.* **6**, 2305.17173 (2023), 2305.17173.
- [4] A. Amon et al. (DES), *Phys. Rev. D* **105**, 023514 (2022), 2105.13543.
- [5] M. Asgari et al. (KiDS), *Astron. Astrophys.* **645**, A104 (2021), 2007.15633.
- [6] D. Brout et al., *Astrophys. J.* **938**, 110 (2022), 2202.04077.
- [7] T. M. C. Abbott et al. (DES), *Astrophys. J. Lett.* **973**, L14 (2024), 2401.02929.
- [8] D. Rubin et al. (2023), 2311.12098.
- [9] A. G. Adame et al. (DESI) (2024), 2404.03002.
- [10] G. Efstathiou (2020), 2007.10716.
- [11] D. Brout and D. Scolnic, *Astrophys. J.* **909**, 26 (2021), 2004.10206.
- [12] E. Mortzell, A. Goobar, J. Johansson, and S. Dhawan, *Astrophys. J.* **935**, 58 (2022), 2106.09400.
- [13] W. L. Freedman, *Astrophys. J.* **919**, 16 (2021), 2106.15656.
- [14] L. Knox and M. Millea, *Phys. Rev. D* **101**, 043533 (2020), 1908.03663.
- [15] E. Di Valentino, O. Mena, S. Pan, L. Visinelli, W. Yang, A. Melchiorri, D. F. Mota, A. G. Riess, and J. Silk, *Class. Quant. Grav.* **38**, 153001 (2021), 2103.01183.
- [16] E. Abdalla et al., *JHEAp* **34**, 49 (2022), 2203.06142.
- [17] V. Poulin, K. K. Boddy, S. Bird, and M. Kamionkowski, *Phys. Rev. D* **97**, 123504 (2018), 1803.02474.
- [18] M. Raveri, *Phys. Rev. D* **101**, 083524 (2020), 1902.01366.
- [19] G. Benevento, W. Hu, and M. Raveri, *Phys. Rev. D* **101**, 103517 (2020), 2002.11707.
- [20] F. McCarthy and J. C. Hill, *Phys. Rev. D* **108**, 063501 (2023), 2210.14339.
- [21] L. Pogosian, M. Raveri, K. Koyama, M. Martinelli, A. Silvestri, G.-B. Zhao, J. Li, S. Peirone, and A. Zucca, *Nature Astron.* **6**, 1484 (2022), 2107.12992.
- [22] V. Poulin, T. L. Smith, R. Calderón, and T. Simon (2024), 2407.18292.
- [23] K. Jedamzik and L. Pogosian, *Phys. Rev. Lett.* **125**, 181302 (2020), 2004.09487.
- [24] L. Thiele, Y. Guan, J. C. Hill, A. Kosowsky, and D. N. Spergel, *Phys. Rev. D* **104**, 063535 (2021), 2105.03003.
- [25] M. Rashkovetskyi, J. B. Muñoz, D. J. Eisenstein, and C. Dvorkin, *Phys. Rev. D* **104**, 103517 (2021), 2108.02747.
- [26] N. Lee, Y. Ali-Haïmoud, N. Schöneberg, and V. Poulin, *Phys. Rev. Lett.* **130**, 161003 (2023), 2212.04494.
- [27] G. P. Lynch, L. Knox, and J. Chluba, *Phys. Rev. D* **110**, 063518 (2024), 2404.05715.
- [28] G. P. Lynch, L. Knox, and J. Chluba (2024), 2406.10202.
- [29] L. Pogosian, G.-B. Zhao, and K. Jedamzik, *Astrophys. J. Lett.* **973**, L13 (2024), 2405.20306.
- [30] K. Jedamzik, L. Pogosian, and G.-B. Zhao, *Commun. in Phys.* **4**, 123 (2021), 2010.04158.
- [31] W. Hu and N. Sugiyama, *Astrophys. J.* **471**, 542 (1996), astro-ph/9510117.
- [32] L. Hart and J. Chluba (2019), 1912.04682.
- [33] S. Seager, D. D. Sasselov, and D. Scott, *Astrophys. J. Lett.* **523**, L1 (1999), astro-ph/9909275.
- [34] W. Y. Wong, A. Moss, and D. Scott, *Mon. Not. Roy. Astron. Soc.* **386**, 1023 (2008), 0711.1357.
- [35] S. Seager, D. D. Sasselov, and D. Scott, *RECFAST: Calculate the Recombination History of the Universe*, Astrophysics Source Code Library, record ascl:1106.026 (2011).
- [36] A. Lewis, A. Challinor, and A. Lasenby, *Astrophys. J.* **538**, 473 (2000), astro-ph/9911177.
- [37] K. Jedamzik, T. Abel, and Y. Ali-Haïmoud (2023), 2312.11448.
- [38] J. Torrado and A. Lewis, *JCAP* **05**, 057 (2021), 2005.05290.
- [39] J. Torrado and A. Lewis, *Cobaya: Bayesian analysis in cosmology*, Astrophysics Source Code Library, record ascl:1910.019 (2019).
- [40] E. Rosenber, S. Gratton, and G. Efstathiou, *Mon. Not. Roy. Astron. Soc.* **517**, 4620 (2022), 2205.10869.
- [41] N. Aghanim et al. (Planck), *Astron. Astrophys.* **641**, A6 (2020), [Erratum: *Astron. Astrophys.* 652, C4 (2021)], 1807.06209.
- [42] H. Prince and J. Dunkley, *Phys. Rev. D* **105**, 023518 (2022), 2104.05715.
- [43] D. J. Eisenstein et al. (SDSS), *Astrophys. J.* **633**, 560 (2005), astro-ph/0501171.
- [44] J. Carron, M. Mirmelstein, and A. Lewis, *JCAP* **09**, 039 (2022), 2206.07773.
- [45] L. Balkenhol et al. (SPT-3G), *Phys. Rev. D* **108**, 023510 (2023), 2212.05642.
- [46] S. Aiola et al. (ACT), *JCAP* **12**, 047 (2020), 2007.07288.
- [47] M. Zaldarriaga and D. D. Harari, *Phys. Rev. D* **52**, 3276 (1995), astro-ph/9504085.
- [48] S. Galli, L. Pogosian, K. Jedamzik, and L. Balkenhol, *Phys. Rev. D* **105**, 023513 (2022), 2109.03816.
- [49] P. Ade et al. (Simons Observatory), *JCAP* **02**, 056 (2019), 1808.07445.
- [50] K. Abazajian et al. (2019), 1907.04473.